JCTC Journal of Chemical Theory and Computation

pubs.acs.org/JCTC Article

Complementing Adiabatic and Nonadiabatic Methods To Understand Internal Conversion Dynamics in Porphyrin Derivatives

Published as part of Journal of Chemical Theory and Computation special issue "First-Principles Simulations of Molecular Optoelectronic Materials: Elementary Excitations and Spatiotemporal Dynamics".

Pavel S. Rukin, Mariagrazia Fortino, Deborah Prezzi,* and Carlo Andrea Rozzi*

Cite This: https://doi.org/10.1021/acs.jctc.4c00698

ABSTRACT: We analyze the internal conversion dynamics within the Q_y and Q_x excited states of both bare and functionalized porphyrins, which are known to exhibit significantly different time constants experimentally. Through the integration of two complementary approaches, static calculation of per-mode reorganization energies and nonadiabatic molecular dynamics, we achieve a comprehensive understanding of the factors determining the different behavior of the two molecules. We identify the key normal and essential modes responsible for the population transfer between excited states and discuss the efficacy of different statistical and nonstatistical analyses in providing a full physics-based description of the phenomenon.

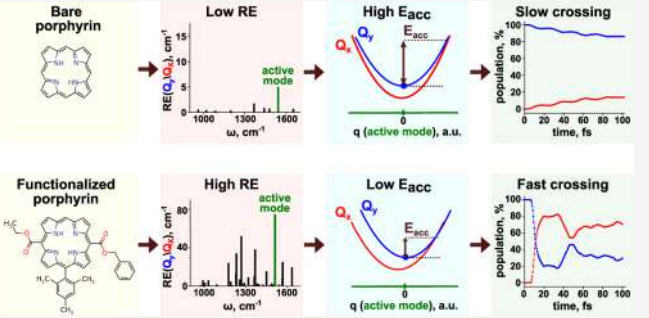

INTRODUCTION

Comprehending internal conversion (IC) is essential for interpreting and forecasting photophysical processes in organic molecules, as it entails the nonradiative transfer of energy from an excited state to another electronic state with lower energy and the same spin multiplicity.[1] This task is particularly challenging as IC is driven by a variety of mechanisms, such as the relative location of potential energy surfaces (PES) in the molecular configurations space, coupling between vibrational modes and between electronic and vibrational degrees of freedom, and anharmonicity,[2,3] just to mention some of intramolecular origin.

In many cases, only a few vibrational modes are actively involved in the IC process, whereas the majority of the modes are just spectators, as also happens in other photoinduced phenomena (charge transfer or delocalization, photoisomerization, etc.). Isolating the vibrational modes that drive the IC process and understanding the connection between molecular structure, vibrational spectrum of the excited states and other factors affecting IC is particularly important, as it might also be exploited for the systematic design of efficient photoactive compounds.[4]

Simplified assumptions, such as the Born−Oppenheimer approximation and the Franck−Condon principle,[5−7] are often employed to rationalize the IC complexity and facilitate calculations of IC rates and characteristic spectroscopic features. In most cases, these assumptions enable the creation of a static representation of the electronic levels involved in IC, the PES inspection at a glance, and the quantification of the role of vibrations through one or a few parameters. One example is the total reorganization energy, which indicates the energy needed for a given configurational change of the system and is commonly adopted in other contexts (such as charge-transfer reactions).[8]

However, in other cases, taking into account nonadiabatic coupling is necessary, especially when dealing with IC between two excited states to describe spectroscopic features linked to non-Condon mechanisms.[2,9−11] The advent of time-resolved spectroscopy and atto-second science has revolutionized the study of IC processes, allowing researchers to exploit electron wave packet dynamics and time-dependent spectroscopies to gain a deeper understanding of IC close to conical intersections.[12−15] These points are particularly critical for IC, as they enable the system to transition almost instantaneously from one electronic state to the other, dramatically reducing the IC time.

Various methods, ranging from classical to fully quantum treatment of the nuclei, have been developed for nonadiabatic molecular dynamics (NAMD), offering a comprehensive view

Received: May 31, 2024
Revised: October 7, 2024
Accepted: October 7, 2024

https://doi.org/10.1021/acs.jctc.4c00698
J. Chem. Theory Comput. XXXX, XXX, XXX−XXX

of the evolution of both electronic orbitals and nuclear trajectories during IC and other photophysical or photochemical phenomena (see refs 16 and 17 for a more extensive discussion). These methods require considerable computational costs, but the ab initio (or quasi ab initio) nature of NAMD enables the exploration of intricate dynamic behaviors without the need for heavy simplifications.

However, performing NAMD simulations from scratch may not be essential or efficient when the goal is to quickly scan the vibrational modes and identify the ones mostly affecting IC.[18,19] Indeed, for instance, protein dynamics in physiological conditions may exhibit diffusion across multiple minima,[20,21] whereas smaller molecules are expected to show minimal configurational changes. It is therefore reasonable to restrict the problem to the domain of small fluctuations around a single local harmonic minimum, particularly on a short time scale.

Either way, statistical methods were specifically developed to analyze the NAMD trajectories. Prominently, essential dynamics (ED),[22] a derivative of principal component analysis (PCA),[23] is particularly tailored to compress the information contained in long equilibrium trajectories of large biomolecules,[24−27] for which it is fair to assume that the subunits showing the largest conformational changes (i.e., the largest variance) are also the most relevant for the physics being simulated. Such techniques, and others, machine learning-based, have evolved and perfected also to detect nonlinear correlations (for an overview see refs 28 and 29 and references therein) and to understand the collective motion of a large number of bath modes.[30] ED alone, however, might not offer the most physically meaningful information in order to fully clarify the functional dynamics of small molecules. The need for complementary approaches to characterize the most relevant atomic motion was recognized, e.g. while studying situations in which intersystem-crossing competes with IC.[31,32] It was soon realized that normal modes and essential modes provide very different kinds of information.[33,34] Below, we will employ ED to identify the main nuclear fluctuations taking part in an IC process, but we will show how it can be backed up with normal-mode analysis to enable a comprehensive interpretation of the intricacy of trajectory ensembles.

Porphyrin derivatives represent an ideal test-bed to study the effect of vibronic coupling on the IC dynamics in small, yet relevant compounds by means of complementary approaches. Indeed, the photophysics of porphyrin derivatives, including chlorophyll, has been the subject of extensive ab initio theoretical studies.[9,35−42] With few exceptions,[32,34,41−43] these investigations usually adopt either a quantum-chemical approach, mostly directed to determine the electronic structure and vibronic effects, or a molecular dynamics approach, mostly focused on following the atomic trajectories. The first approach is typically static, resting on very accurate electronic structure calculations performed on a few atomic configurations and smaller systems, treating at a later stage the coupling with vibrations.[9,35,36] The second approach results in explicit time-dependent simulations, highlighting dynamical features,[37−40] struggling for the balance between accuracy and the effects of electron-nuclei couplings simultaneously active throughout many different time and energy scales.

Here, we challenge a simple yet effective static analysis based on first-principles adiabatic PES and per-mode reorganization energies (REs) recently demonstrated on porphyrins[19] and compare its outcomes to explicit NAMD simulations and ED analysis. The workflow we propose can be applied to study ultrafast IC and similar processes in a completely general way. It is independent of the underlying level of theory adopted to describe the electronic structure and the molecular dynamics. It rests on clear and simple assumptions (meant to make the analysis stage plainer), which, however, can be falsified, to some extent, within the procedure itself (see Methods section).

As a way of benchmarking the method, and without loss of generality, we chose to study two different molecules, i.e., the bare porphyrin molecule (BP) and a functionalized variant (FP) depicted in Figure 1,[44−48] for which ultrafast IC between

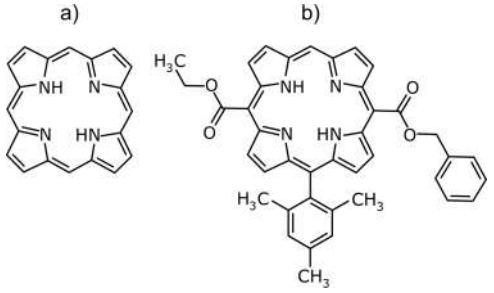

Figure 1. Molecular structures of bare (a) and functionalized (b) porphyrin.

the S_2 and S_1 excited states corresponding to the Q_y and Q_x spectral bands has been recently observed by means of ultrafast two-dimensional spectroscopy, with substantially different estimated IC times (∼60 and ∼150 fs for FP[18] and BP,[49] respectively). In this way, we provide a true-positive case scenario, useful to highlight the strengths and limitations of the proposed procedure.

We examined the differences in the evolution of excited states of the two molecules within the first 100 fs. We show how to complement and relate single-point adiabatic quantum-chemical methods and dynamical nonadiabatic simulations to gain a deeper awareness of the effects of porphyrin functionalization on its IC dynamics. We demonstrate that a simple preliminary scan of the REs of the excited-state normal modes can be profitably used as a guide for subsequent time-dependent simulations. On the other hand, we show that a full nonadiabatic treatment is necessary to complete the view of IC in all its details.

METHODS

Our analysis combines per-mode RE obtained from the adiabatic PES with the time-dependent evolution of the excited states populations, enriched with essential modes analysis for the nonadiabatic excited-state molecular dynamics (NA-ESMD) trajectories. The major calculation steps are explained in the following subsections, whereas the overall schematic workflow is shown in Figure 2.

Adiabatic PES and Per-mode RE. In principle, our approach allows one to employ any first-principle method of choice to calculate the PES. Here, we have obtained all electronic structure calculations at the DFT/TD-DFT level ignoring spin−orbit interaction, i.e., restricting the calculation to the singlet manifold. Specifically, optimized geometries and frequency calculations for ground and excited states were performed using the CAM-B3LYP functional on the 6-311G(d,p) basis set at both the DFT and TDDFT levels. The effect of solvent was taken into account by applying the

https://doi.org/10.1021/acs.jctc.4c00698
J. Chem. Theory Comput. XXXX, XXX, XXX−XXX

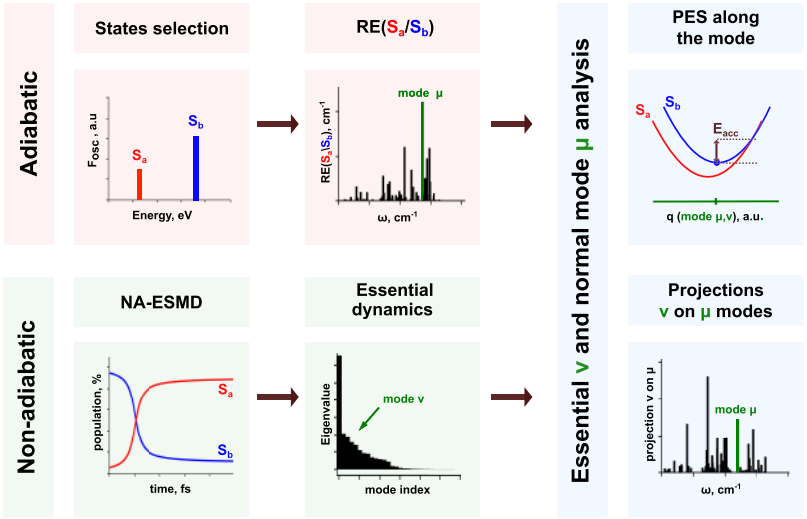

Figure 2. Schematic workflow of the calculations. In the adiabatic part (light red) of our approach, the excited states and the corresponding REs are calculated to define the relevant (i.e., most vibronically active) normal modes (μ) of the system. The nonadiabatic part (light green) consists of NAMD simulations and essential mode (ν) analysis. The analysis of essential and normal modes (light blue) comprises: (1) PES scans along these modes to find crossing points and access energy barriers (E_{acc}); (2) projections of essential modes on normal ones to correlate adiabatic and nonadiabatic analyses.

continuum solvation model (PCM)[50] for tetrahydrofuran as in previous studies,[18,19] thereby neglecting the coupling between solvation and electronic correlation. DFT and TDDFT calculations were performed by using the Gaussian16 package.[51] For the full technical details of these calculations, we refer the reader to Rukin et al.[19]

In the second step, in order to ease as much as possible the estimation of the RE, we employ a linear coupling model (i.e., the independent mode, displaced harmonic oscillator model[52−56]). Thus, the displacement along the mode between the PES of the two states involved, S_a and S_b, is the single most relevant parameter. This approach is exact when anharmonicities and Duschinsky effects[57,58] can be neglected, and it has been successfully applied to describe different photophysical phenomena, including IC in several scenarios.[4,18,53−56,59,60] However, the validity of the latter assumptions is not assumed a priori, as if we postulated a model Hamiltonian in the first place (see, e.g., refs 57, 61, and 62.), but it can instead be cross-checked to some extent, on the basis of the underlying accurate first-principle step. For example, the harmonicity of individual PES can be checked to determine the maximum amplitude of the oscillations for which deviation from harmonicity is acceptable.

The advantage of this simplified approach consists in the fact that it is straightforward to calculate the displacement Δq_μ^{ab} between the minima of two PES, S_a and S_b, for each mode $\mu \in [1, \cdots, 3N-6]$ as

$$\Delta q_\mu^{ab} = -\frac{g_\mu^b}{M_\mu \omega_\mu^2} \tag{1}$$

where g_μ^b is the gradient of the state S_b, calculated at the coordinate corresponding to the equilibrium geometry of the state S_a; ω_μ and M_μ are the frequencies and the reduced mass of the the μ-th normal mode. From these quantities the dimensionless Huang−Rhys (HR) factors ξ_μ and the RE E_μ for each mode can be written, respectively, as

$$\xi_\mu = \frac{1}{2\hbar} M_\mu (\Delta q_\mu^{ab})^2 \omega_\mu \tag{2}$$

$$E_\mu = \xi_\mu \hbar \omega_\mu \tag{3}$$

HRs and REs are obtained from the above-mentioned ab initio DFT and TDDFT calculations, where we computed energy gradients g_μ^b at the coordinate of the optimized geometry of the state S_a, as well as S_a-state normal modes from the diagonalization of the corresponding Hessian matrix.

As a final remark, we note that although dimensionless HR factors are more commonly used to quantify vibronic coupling in general, in our context, where the absolute energetics of the PES are of interest, we prefer to use per-mode RE as they directly point at the energy difference between the S_a equilibrium geometry and the excited state S_b minimum for each mode: the normal modes having the largest RE are the ones most likely affecting the transition from S_a to S_b via vibronic coupling.

Nonadiabatic Excited-State Dynamics. Next, we explore the excited-state dynamics by populating the higher energy S_b excited state and allowing for nonadiabatic trajectory switching through the Fewest Switches Surface Hopping (FSSH) mechanism.[63,64] NA-ESMD[17,40] calculations are performed by evolving the system in time from a statistical ensemble of ground state atomic configurations, dispersed according to a Wigner distribution[65] at room temperature. NA-ESMD is combined with real-time analytical computations of excited-state energies, gradients, and nonadiabatic couplings (NAC), performed in the TDDFT framework, where the electronic wave functions used to compute the NAC between any pair of states are based on Casida's auxiliary multielectron wave functions.[66,67]

The trajectories generated during NA-ESMD simulations are used to extract the average nonadiabatic population of the involved states as a function of time. Additionally, excited-state energy levels have been computed for each trajectory as well as averaged over all computed trajectories to obtain ensemble-averaged PES. From the joint inspection of time-dependent

https://doi.org/10.1021/acs.jctc.4c00698
J. Chem. Theory Comput. XXXX, XXX, XXX−XXX

populations and PES, the existence of conical intersections or avoided crossings enabling ultrafast transitions between the states of interest can be inferred. However, for a more in-depth comprehension of the effect of individual modes, further statistical analyses are required. To that end, we resort to ED and trajectory projection techniques. ED is a widespread technique used to compress multidimensional data sets to their most significant components.[22,23,26,28,68] When applied to an ensemble of trajectories, it consists of the principal components of the atomic coordinate displacement with respect to a reference structure in a given time frame.

While it is customary, e.g., in the case of long equilibrium trajectory of biomolecules, to calculate atomic displacements with respect to the temperature-averaged ground state configuration, here, we opt for the lower energy S_a configuration as a reference point, as we are interested in studying the IC between the two excited states, S_b and S_a. Calling $\{\mathbf{x}^a\}$ the column vector of the $3N$ Cartesian components of the atomic positions of the system at this configuration, we adopt the short notation $\mathbf{x}_j(t) = \{\mathbf{x}(t)\}_j - \{\mathbf{x}^a\}$ to indicate the time-dependent relative displacement vector for the j-th trajectory in the simulation ensemble $j \in [1, \cdots, N_{tr}]$. Next, we define the average trajectory at each time

$$\mathbf{x}(t) = \frac{1}{N_{tr}} \sum_{j=1}^{N_{tr}} \mathbf{x}_j(t) \tag{4}$$

For a given time interval T − corresponding either to the whole simulation time or to any relevant subinterval−we can then calculate the time-averaged mean displacement

$$\overline{\mathbf{x}} = \frac{1}{T} \int_0^T \mathbf{x}(t)\mathrm{d}t \tag{5}$$

which is used to construct the covariance matrix of size $(3N)^2$, as in ref 23.

$$\mathbf{C} = \frac{1}{T} \int_0^T [\mathbf{x}(t) - \overline{\mathbf{x}}][\mathbf{x}(t) - \overline{\mathbf{x}}]^{\mathrm{T}}\mathrm{d}t \tag{6}$$

Diagonalization of the $\mathbf{C}$ matrix by an orthogonal coordinate transformation $\mathbf{L}$ modifies $\mathbf{C}$ into the diagonal matrix $\mathbf{\Lambda}$ of the eigenvalues λ_ν

$$\mathbf{\Lambda} = \mathbf{L}^T\mathbf{C}\mathbf{L} \tag{7}$$

The columns of the matrix $\mathbf{L}$ are the eigenvectors $\mathbf{L}_\nu$ corresponding to λ_ν. The ED is obtained by selecting principal components corresponding to the first k largest eigenvalues (usually just a few) and calculating their weights

$$w_\nu = \frac{\lambda_\nu}{\sum_{i=1}^{3N} \lambda_i} \tag{8}$$

depending on the desired amount of compression one wishes to achieve. It is important to realize that both λ_ν and $\mathbf{L}_\nu$ depend on the chosen time frame T, and thereby so do w_ν.

All NA-ESMD simulations were carried out by using the NEWTON-X package[69] and associated scripts.[70] NEWTON-X was linked to the Gaussian16 package[51] for on-the-fly computations of electronic properties during dynamics propagation. The electronic calculations have been performed at the CAM-B3LYP/6-311G(d,p) level of theory, the same as used for the static investigation. We prepared $N_{tr} = 100$ replicas of the systems by populating their second excited electronic state, i.e., the Q_y state. Each NA-ESMD trajectory was evolved for a total simulation time of 100 fs with a time step of 0.5 fs. Further details relevant to calculation reproducibility are reported in the Supporting Information.

Analysis of the Trajectories. In order to relate the ED with the normal modes identified as the most active by the preliminary per-mode RE study, we can construct the PES sections along both essential and normal modes. These PES sections provide an interpretation of the nonadiabatic relaxation mechanism. Here, the μ-th modal displacement Δq_μ is expressed in Cartesian components by the linear relation[19]

$$\Delta\mathbf{X}_\mu = \frac{1}{\sqrt{M_\mu}}\mathbf{L}_\mu \Delta q_\mu \tag{9}$$

Starting from the initial configuration $\mathbf{X}(0)$, typically located at the ground state PES minimum, the deformed configurations following the μ-th (either normal or essential) mode are

$$\mathbf{X}(\Delta q_\mu) = \mathbf{X}(0) + \Delta\mathbf{X}_\mu \tag{10}$$

At each $\mathbf{X}(\Delta q_\mu)$ the vertical excitations are computed to the excited state PES, quantifying the energy gap between the PES.

To understand the correlation between modes obtained through dynamic nonadiabatic and static adiabatic approaches, we can express a selected ν-th essential mode in terms of the μ-th normal mode by projecting its eigenvector $\mathbf{L}_\nu$ on $\mathbf{L}_\mu$

$$P_{\mu\nu} = \frac{\mathbf{L}_\nu^{\mathrm{T}}\mathbf{L}_\mu}{||\mathbf{L}_\mu||} \tag{11}$$

To quantify the weight of each normal mode in the essential mode, we use the normalized squared projection

$$W_{\mu\nu} = \frac{P_{\mu\nu}^2}{\sum_\mu P_{\mu\nu}^2} \tag{12}$$

RESULTS AND DISCUSSION

By simply looking at the molecular structures in Figure 1, it is not immediately evident what causes the observed doubling of the IC rate when the side connectors and spacers subunits are added to the main conjugated ring. The addition of ethoxycarbonyl connectors to the BP structure (Figure 1) only slightly affects the vertical excitation energies. Indeed, the FP vertical excitation energies of the Q band are red-shifted by just about 10 meV with respect to BP, while the Q_x/Q_y gap is almost unchanged, as reported in ref 19. Although it is reasonable to expect a modification in the symmetry and localization of the charge density of the excited state, it is clear that there is no major effect on the electronic structure of the molecule overall. However, the side groups do affect the normal modes of vibration[19] in a complex way. Specifically, while some modes can still be mapped onto the modes of the conjugated BP backbone, others are entirely new in shape and/or localization.

Adiabatic PES and Per-mode RE. In this section, we briefly summarize the main features emerging from our static adiabatic analysis,[19] where per-mode REs are coupled to scans of the excited-state PES along selected modes to gain information on the vibrations affecting IC. More details can be found in refs 18 and 19. Figure 3 shows the REs based on the relative displacement of the Q-band excited states (Q_x and Q_y) computed for BP (a) and FP (c), respectively. The

https://doi.org/10.1021/acs.jctc.4c00698
J. Chem. Theory Comput. XXXX, XXX, XXX−XXX

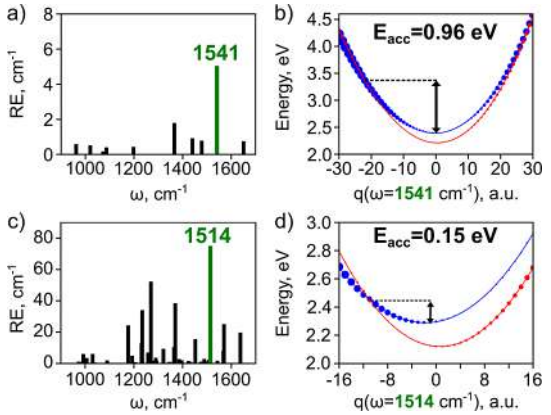

Figure 3. (a, c) Q_x/Q_y REs for BP (a) and FP (c), respectively. (b, d) Section of the PES along the most active Q_x mode in the range [900, 1700] cm^{-1} for BP (b) and FP (d), respectively. Here, q = 0 corresponds to the ground state geometry. Red color is used for Q_x PES, and blue for Q_y. The size of the circles is proportional to their relative oscillator strength. E_{acc} indicates the maximum energy barrier from the Q_y minimum to the Q_x−Q_y crossing point.

selected set of modes is obtained from the lowest excited state Q_x. Green bars indicate the normal modes with the highest RE for each case, which are hereafter called *active modes*. REs are here plotted in the relevant range [900, 1700] cm^{-1}, while the full wavenumber range ([0, 3600] cm^{-1}) is displayed (Figure S1) and thoroughly discussed in the Supporting Information. Figure 3 also displays the PES of BP (b) and FP (d), respectively, as obtained by displacement along each active mode (eqs 9 and 10). It is worth mentioning that, while REs and PES are computed with respect to Q_x modes, here the PES are displayed by setting q = 0 to the ground state minimum from where the system is initially excited.[71] This choice is made to ease the comparison with nonadiabatic trajectories discussed below.

As can be noted by comparing the results for BP and FP, REs display an overall increase for the whole range of frequencies due to functionalization. This indicates that the displacements of the Q_y and Q_x PES are larger in the case of FP than for BP. To confirm this, we plotted the Q_y and Q_x PES along the highest-RE mode in the [900, 1700] cm^{-1} frequency range for each structure (see Figure 3b for the 1541 cm^{-1} BP mode and Figure 3d for the 1514 cm^{-1} FP mode). Defining the access energy (E_{acc}) along the active mode as the maximum energy barrier to the crossing point between Q_y and Q_x (computed from the local minimum of Q_y), we thus find that E_{acc} is much smaller for the system with higher RE. Specifically, the RE of the FP active mode is 15 times higher than the one of BP, with a correspondingly lower E_{acc} for FP (∼0.15 eV) than for BP (∼0.96 eV).

To conclude, by computing REs and analyzing the PES along a single normal mode, our analysis suggests that IC would occur on a shorter time scale in FP than in BP thanks to the lower access barrier. In addition, this analysis allows us to identify the modes mostly affecting the IC process according to the static picture.

Population Dynamics. To prove the picture gained from REs and normal modes analysis, we simulated 100 fs of nonadiabatic time evolution of both BP and FP starting in their fully populated Q_y states in an ensemble of 100 trajectories. The time-dependent excited state population and energy profile averaged over all trajectories are reported in Figure 4 for both molecules; individual trajectories and their energy profiles can be found in the Supporting Information (Figure S2).

In the case of BP, the population dynamics (Figure 4a) clearly show a negligible interaction between the states. Indeed, we find that the population of Q_x (red curve) keeps slowly increasing in the first 100 fs, but without overstepping ∼15%, pointing at a very low hopping probability from the higher-energy Q_y state to the lower-energy Q_x (see also Figure S2). Correspondingly, the averaged energy levels of Q_x (red) and Q_y (blue) (Figure 4c) do not show any noticeable changes, i.e., $E_{Q_y} - E_{Q_x} \sim$ constant.

Please note that this scenario only holds when the Q_y state (and no other) is initially populated, for which we can infer an IC time of several hundreds of fs. Experimentally, however, the Q-band IC is usually probed by populating the B band first (see ref 49), which leads to a different mechanism, and to faster IC of the order of 150 fs proceeding through a conical intersection of the B state with Q states, as explained in ref 41. Here, we populate only the Q_y state of BP in order to compare

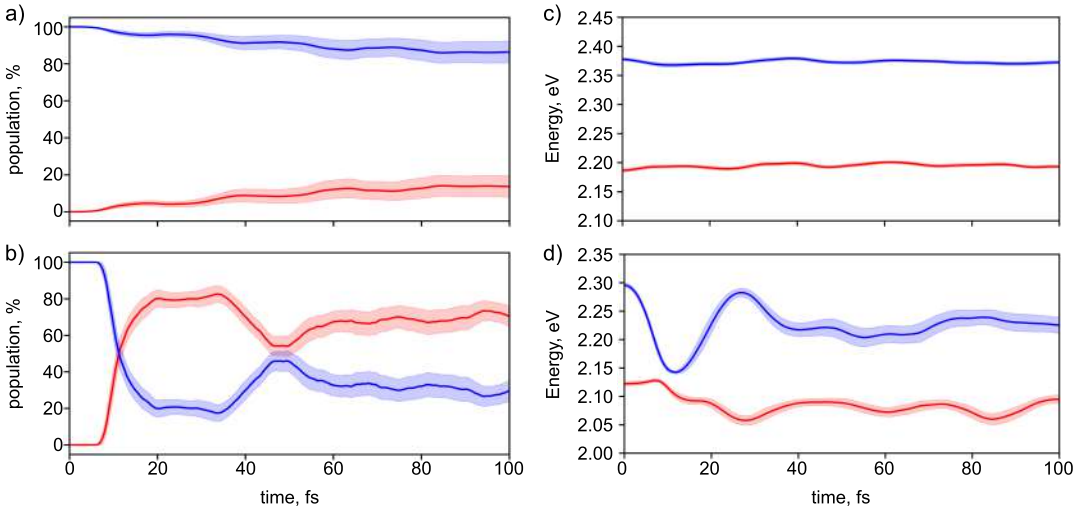

Figure 4. Time evolution of the ensemble-averaged populations (a, b) and electronic energy levels (c, d) of Q_x (red) and Q_y (blue) states for bare (a, c) and functionalized (b, d) porphyrin. The shaded bands indicate 99% confidence intervals.

https://doi.org/10.1021/acs.jctc.4c00698
J. Chem. Theory Comput. XXXX, XXX, XXX−XXX

the simulations for FP and BP on an equal footing. As such, our results for BP cannot be directly compared with experiments considering B-band excitation. Interestingly, our result, showing an overly long conversion time, could also be considered support of the findings of ref 41, confirming that, if the B population is *not* taken into account, the $Q_y \rightarrow Q_x$ IC of BP would take much longer than the observed one.

The situation is very different in the case of FP (Figure 4b,d), where we find a first crossing of the population curves (panel b) at about 12 fs, with the population of Q_x increasing from 0 up to over 80%, followed by a decrease, with the states reaching almost equal populations after about 45−50 fs. After this second close encounter, the population of Q_x starts to slowly increase again. This pattern indicates that the states are still strongly coupled before 50 fs, as demonstrated also by the behavior of the energy difference between the Q_y to Q_x (Figure 4d): $E_{Q_y} - E_{Q_x}$ reaches a minimum in correspondence with the first crossing of the populations and it tends to stabilize above 40 fs. Noteworthy, the average plot in Figure 4d) might convey the illusion of an avoided crossing because the states are energy sorted in the computation of the averaged energy profiles. Indeed, individual trajectories show that the system goes through a crossing (see Figure S2b) and indicate that the IC process occurs via conical intersections rather than avoided crossing. Overall, our results for FP indicate a strong nonadiabatic interaction between the states in the first 20 fs, leading to surface hopping. Moreover, the characteristic times found here are in excellent agreement with the experimental observation of IC from Q_y to Q_x by means of transient absorption and two-dimensional electronic spectroscopy (2DES) measurements, which is found to occur within 60 fs.[18]

Essential Dynamics. Since the modes extracted from ED (eqs 5−8) depend on the chosen time frame T, we consider here two different ranges for our analysis, i.e., the first 20 fs (T_{20}) and the entire simulation time frame of 100 fs (T_{100}). This allows us to focus on the first stages after the excitation of the molecule, when the first population crossing event takes place in FP (Figure 4), and compare the behavior before and after hopping from the Q_y to the Q_x PES.

Figure 5 shows the relative weights $w_i(T)$ (see eq 8) of the essential modes for both BP and FP, calculated in T_{20} and T_{100}.

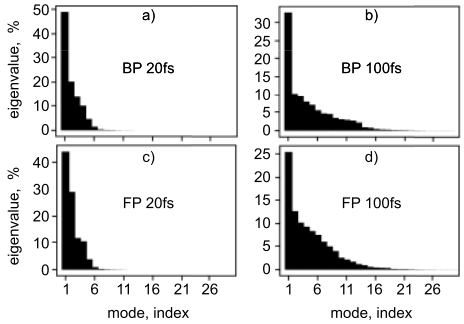

Figure 5. Sorted weights w_ν (eq 8) showing the percentages of the total variance explained by each essential mode, calculated on a 20 fs (a, c) and 100 fs time frame (b, d), for both BP (a, b) and FP (c, d).

In T_{100}, 15 modes can explain 97% of the variance; in T_{20}, just 6 modes are sufficient. A similar result was also previously found for chlorophyll-like systems.[40]

At variance with what is often observed in large protein molecules, the key motions of FP, do not consist in major rearrangements of functionally independent molecular subunits. Therefore, the question arises whether the inspection of the time evolution of the time-dependent relative weights of the essential modes can assist in discerning the different population dynamics observed in BP and FP. The answer to this question is negative. It can be understood by observing Figure 6, which shows the time-dependent standard deviation

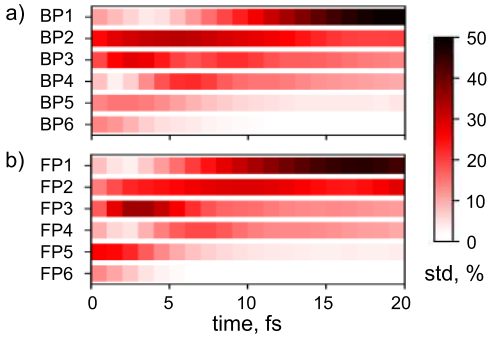

Figure 6. Time-dependent standard deviation of the displacements for the first six essential modes of T_{20}, normalized at each time step and expressed as percentages for BP (a) and FP (b).

values of the first six modes (normalized, in %) for both BP (panel a) and FP (b). A similar analysis on the 100 fs time frame is reported in the Supporting Information (see Figures S3 and S4).

We observe that some modes contribute the most within the first 4−5 fs (BP5−6; FP5−6), others begin to contribute after 5 fs (BP1, BP4; FP1, FP4), and a third set contributes throughout the entire time interval (BP2, BP3; FP2, FP3). Noticeably, without any knowledge of the character of each mode, the patterns for BP and FP look overall similar. Yet, fast IC is observed only for FP. The scenario does not substantially change if we consider mass-weighted coordinates before performing PCA (see Figure S5). This challenges the physical insight actually gained from PCA alone, which does an excellent job at reducing the dimensionality of the problem from a geometrical perspective but does not provide by itself any intuition about the physics driving the dynamics.

The investigation of the energy profiles of Q_x and Q_y states along each most essential mode, reported in Figure 7, helps clarify their different roles in the two molecules. Here, the procedure used to study PES along normal modes (eqs 9 and 10) is applied to essential modes, and the Q_x (red) and Q_y (blue) PES are reported, together with the corresponding atomic displacements (green arrows) for both BP (a) and FP (b). The evaluation of essential mode anharmonicity is reported and discussed in Supporting Information (Table S1).

From the comparison, we clearly find that the relative displacement of Q_x and Q_y PES is completely different for each pair of modes (BP1, FP1) and (BP2, FP2), despite exhibiting similar standard deviation patterns (Figure 6). Indeed, the energy barrier to reach the Q_x−Q_y crossing point, E_{acc}, becomes vanishingly small in the case of FP thanks to the large relative displacement of the states when moving along FP1 and FP2. On the contrary, the PES of Q_x and Q_y are almost undisplaced when considering BP1 and BP2 modes for the bare porphyrin, with $E_{acc} \sim 0.64$ eV and ∼0.86 eV, respectively.

Equipped with the knowledge of which essential modes are responsible for the crossing in FP, we can go back to the

https://doi.org/10.1021/acs.jctc.4c00698
J. Chem. Theory Comput. XXXX, XXX, XXX−XXX

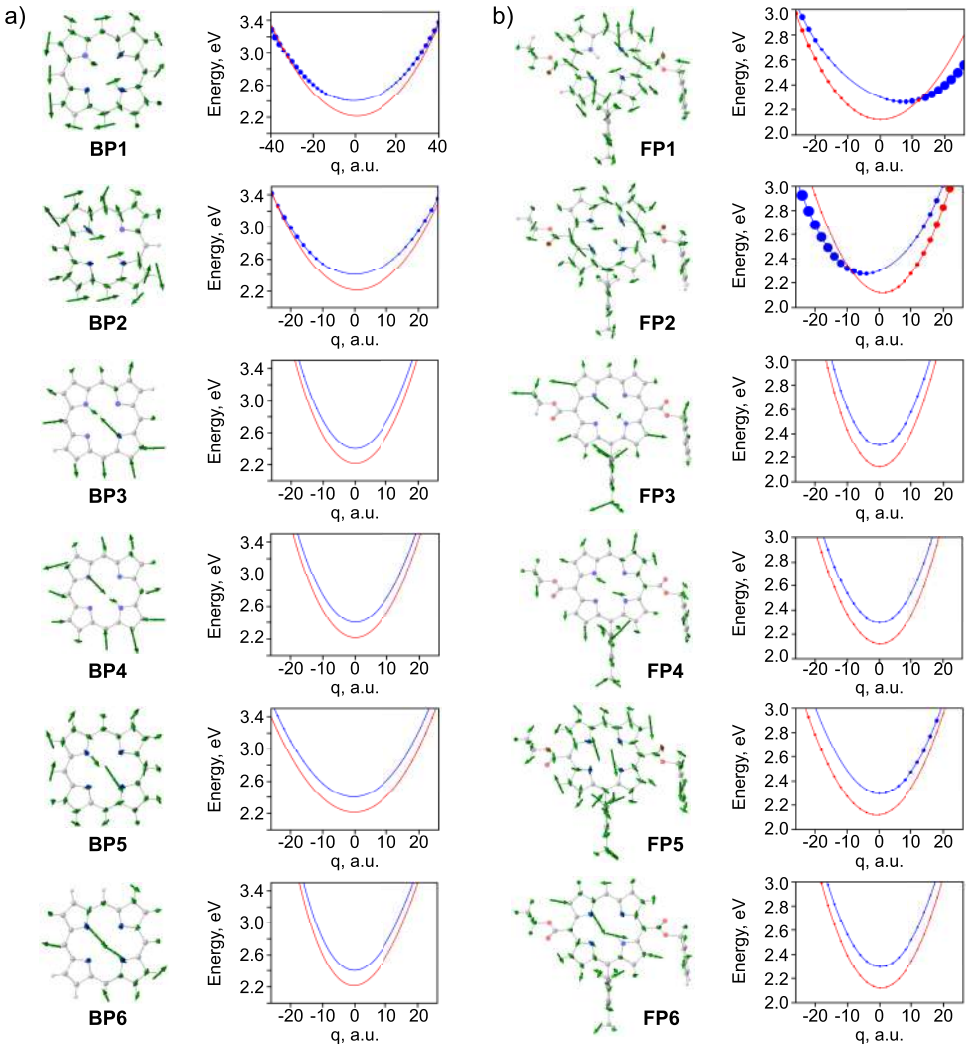

Figure 7. Atomic displacements corresponding to the six most essential modes within the 20 fs time frame for BP (a) and FP (b). Each displacement is accompanied by the PES of the Q_x (red) and Q_y (blue) states along the mode. Here, $q = 0$ corresponds to the ground state geometry. The sizes of the circles depict the oscillator strengths of the transitions for each single-point TDDFT calculation.

analysis of the time-dependent standard deviations (Figure 6). It becomes apparent that FP2 gives the most significant contribution within the first 5 fs, while FP1 starts dominating from about 8−10 fs. Interestingly, the substantial contribution of FP3 (at 3−5 fs) does not lead to any crossing or hopping between the two PES, as indicated by their negligible displacement along this mode.

Extending this analysis to the 100 fs time frame (see Figures S3 and S4) reveals that the essential modes contributing the largest amount of variance (i.e., with the highest eigenvalues λ_i) are not always the most interesting from the point of view of IC physics. In fact, the ED provides compression of information, but does not necessarily convey the relevance of the information itself without further physical examination of the processes involved. In particular, here the time interval in which the events occur is critical: the essential modes corresponding to the full 100 fs interval are dominated by the stationary post-transition dynamics, which has nothing to do with the conversion itself that dominates only the first 20 fs.

For this reason, it is important to couple ED to adiabatic analysis. From inspection of the PES displacements, we indeed notice that certain modes with high eigenvalues (e.g., ^{100}FP1-^{100}FP3, Figure S4) do not significantly impact IC, as they show negligible PES displacement and do not contribute at the first 20 fs of the trajectory (see Figure S4a). On the contrary, other modes with lower eigenvalues show significant PES displacement (e.g., ^{100}FP4, ^{100}FP5, ^{100}FP7, ^{100}FP8, ^{100}FP9, ^{100}FP11, in Figure S4c).

To summarize this section, we stress again the importance of additional PES scanning along the obtained ED modes. It defines their character (displaced or undisplaced) and serves as a step before using time-dependent standard deviation analysis (like in Figure 6). This analysis, consequently, clarifies the time range where the important modes (in our case displaced ones that lead to the energy gap reduction) are active.

Projection of the ED Modes on the QM Normal Modes. After a complete NA-ESMD investigation is performed, it is interesting to go back to the static normal-mode analysis and correlate it with the ED analysis shown above. We thus project the first six essential modes of the 20 fs time frame (see eqs 11 and 12) on the full set of Q_x normal modes. The projections are displayed in Figure 8 for both BP and FP (panels a and b, respectively). Those extracted for the 100 fs time frame are provided in the Supporting Information (Figures S6 and S7).

https://doi.org/10.1021/acs.jctc.4c00698
J. Chem. Theory Comput. XXXX, XXX, XXX−XXX

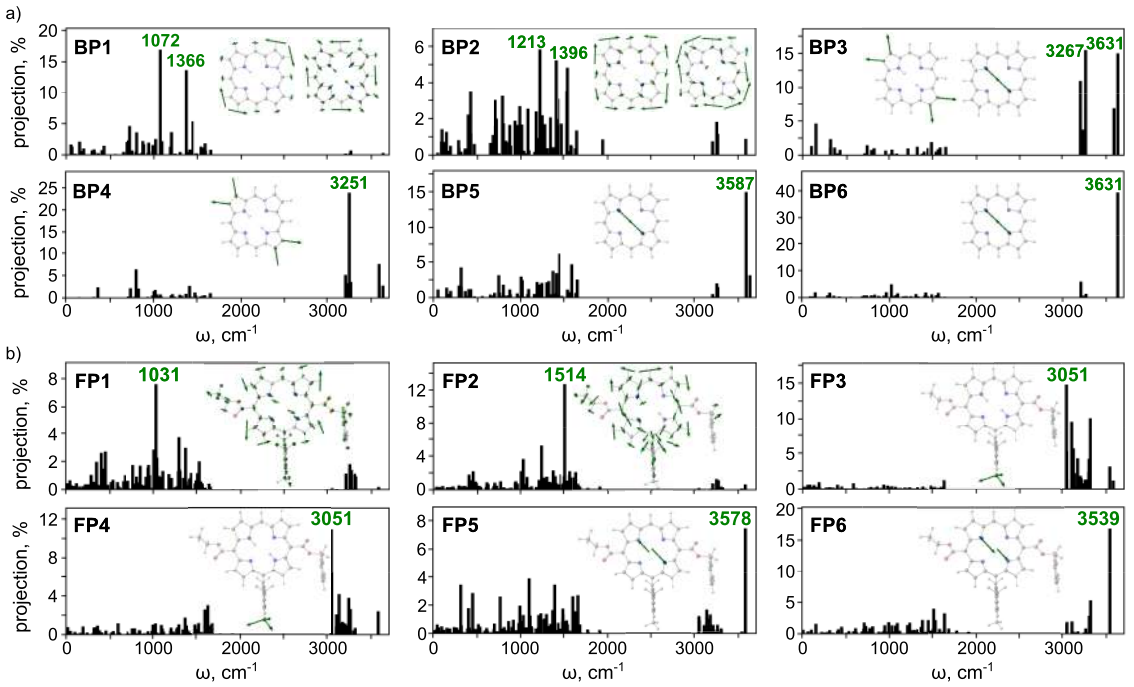

Figure 8. Projections (see eqs 11 and 12) of the essential modes within the 20 fs time frame on the Q_x normal modes of BP (a) and FP (b). Atomic displacements of the Q_x normal modes mostly contributing to each essential mode are depicted in the plots, and their frequencies are indicated in green.

From inspection of Figure 8, we find that essential modes comprise two types of QM modes for both molecules: delocalized over the porphyrin fragment ([1000, 1600] cm^{-1}, BP1−2 and FP1−2), and localized on X-H type bonds ([3000, 3650] cm^{-1}, BP3−6 and FP3−6). With this in mind and going back to PES displacements (see Figure 7), we note that the PES show small to negligible displacement when fast X-H modes dominate (Figure 7, see BP3−6 and FP3−6), suggesting that they do not contribute to IC. This highlights once again that ED analysis does not tell us anything about the importance of each essential mode to a specific process. As such, while the projection of essential modes on normal modes gives information about their similarity, we need PES analysis to determine whether each mode is actually coupled to any electronic excitation.

From the same analysis, we instead find larger displacements arising when delocalized modes contribute the most (see BP1−2 and FP1−2 in Figures 7 and 8), also leading to a reduction of E_{acc}. Focusing on the character of these two most essential modes, we note in particular that BP1 and BP2 predominantly consist of rocking vibrations of H atoms, whereas FP1 and FP2 additionally feature contributions from C atoms of the porphyrin fragment. Notably, Figure 8 shows that the most prominent contribution to FP2 is indeed given by the 1514 cm^{-1} normal mode, which was earlier predicted to be one of the most *active* modes according to RE and static analysis (see ref 19 and Figure 3c). Moreover, this mode was also observed experimentally by means of transient absorption and 2DES.[18]

On the contrary, the normal mode at 1031 cm^{-1}, mostly contributing to FP1, is not indicated as one of the most active in the static analysis. One reason for this lack could lie in the fact that we considered only the modes of the Q_x excited state. A more complete picture would arise if the modes of Q_y could also be included. However, this was not possible due to an optimization failure. The problem arose because the minimum of the Q_y state is close to the crossing point, as can be seen in the scan of FP1 in Figure 7.

CONCLUSIONS

A fully complementary scheme (see Figure 2) for investigating IC was developed, integrating the typically separate static adiabatic and dynamic NA-ESMD approaches. This scheme was applied and validated on bare porphyrin and its functionalized variant FP. The choice of these molecules does not restrict the applicability of our method. They were chosen mainly because recent state-of-the-art 2D spectroscopy shows that they exhibit very different IC rates, providing an ideal true-positive identification case. We show that normal-mode analysis, paired with the computation of per-mode RE, can serve as a preliminary, approximate yet quick and effective step in investigating IC close to conical intersections in terms of access energy. The E_{acc} value (see Figure 3) serves as a criterion to decide whether further investigation of the system with more computationally demanding dynamics calculations is necessary (in the case of FP), or if the barrier is sufficiently large it is evident that further investigation will not result in fast IC (as for BP).

The population dynamics reveals that, in the case of FP, there is a rapid hopping from the Q_y to the Q_x state at approximately 12 fs, followed by the almost equalization of the population of the states around 45−50 fs. The populations of the first two excited states diverge at a later time, with a gradual increase in the Q_x population and a decrease in the Q_y population. On the other hand, in the case of BP, there is no crossing pattern within the first 100 fs. Instead, there is a slow transfer of population from the Q_y state to the Q_x state. The data obtained from the population dynamics correlates well with previous studies for BP[49] and FP.[18]

https://doi.org/10.1021/acs.jctc.4c00698
J. Chem. Theory Comput. XXXX, XXX, XXX−XXX

We argue that ED, a method widely used for studying proteins on long-time scales, requires special care and must be adapted for studying fast processes, such as ultrafast relaxation, especially in smaller, more rigid molecules. Indeed, this analysis provides essential modes that are not *per se* sufficient to disclose the underlying physics but must be paired with individual modes of PES scanning and RE estimation to understand their specific contributions to the IC process. The joint study of essential modes and normal modes through PES scanning allows us to extract their importance not only through geometric analysis (PCA, see Figures 5 and 6) but also by understanding their influence on reducing the energy gap between the excited states (see Figure 7).

In the end, we demonstrate how essential modes can be linked to normal modes through the projection procedure (see Figure 8). Specifically, in the case of FP, we show that the earlier discovered[18,19] specific normal mode at 1514 cm^{-1} prominently appears in the essential mode FP2 (see Figure 7), which leads to the crossing. However, FP1, another essential mode that brings the system to the crossing, is not predicted by normal-mode analysis. This demonstrates that these methods should be employed together to conduct a comprehensive study of the IC process and to possibly design photoactive molecules with optimal IC dynamics.

■ ASSOCIATED CONTENT

Supporting Information

The Supporting Information is available free of charge at https://pubs.acs.org/doi/10.1021/acs.jctc.4c00698.

Calculation details of the per-mode RE and additional PES for the low-frequency modes of BP and FP (Figure S1); individual trajectories for BP and FP (Figure S2), including the calculation details of the FSSH mechanism; interpolation details of the PES and anharmonicity coefficients (Table S1); ED for the full 100 fs trajectories for both BP and FP (Figures S3 and S4); comparison between nonweighted and mass-weighted coordinates to extract essential modes (Figure S5); and projections of the obtained essential modes onto the normal ones (Figures S6 and S7) (PDF)

■ AUTHOR INFORMATION

Corresponding Authors

Deborah Prezzi − *Istituto Nanoscienze − CNR, 41125 Modena, Italy;* orcid.org/0000-0002-7294-7450; Email: deborah.prezzi@nano.cnr.it

Carlo Andrea Rozzi − *Istituto Nanoscienze − CNR, 41125 Modena, Italy;* orcid.org/0000-0001-6429-4835; Email: carloandrea.rozzi@nano.cnr.it

Authors

Pavel S. Rukin − *Istituto Nanoscienze − CNR, 41125 Modena, Italy;* orcid.org/0000-0002-9408-2793

Mariagrazia Fortino − *Dipartimento di Scienze della Salute, Università di Catanzaro, 88100 Catanzaro, Italy*

Complete contact information is available at: https://pubs.acs.org/10.1021/acs.jctc.4c00698

Notes

The authors declare no competing financial interest.

■ ACKNOWLEDGMENTS

This work was supported by the Next Generation EU PRIN 2022 grant no. 202284JP34 − VIBETWO and by the Italian Ministry of University and Research, within the program PRIN 2017, grant no. 201795SBA3 − HARVEST. The authors acknowledge the CINECA award under the ISCRA initiative, for the availability of high-performance computing resources and support.

■ REFERENCES

(1) Oldani, N.; Tretiak, S.; Bazan, G.; Fernandez-Alberti, S. Modeling of internal conversion in photoexcited conjugated molecular donors used in organic photovoltaics. *Energy Environ. Sci.* **2014**, *7*, 1175−1184.

(2) Valiev, R. R.; Merzlikin, B. S.; Nasibullin, R. T.; Kurtzevitch, A.; Cherepanov, V. N.; Ramazanov, R. R.; Sundholm, D.; Kurtén, T. Internal conversion rate constant calculations considering Duschinsky, anharmonic and Herzberg−Teller effects. *Phys. Chem. Chem. Phys.* **2023**, *25*, 6406−6415.

(3) Wang, Y.; Ren, J.; Shuai, Z. Evaluating the anharmonicity contributions to the molecular excited state internal conversion rates with finite temperature TD-DMRG. *J. Chem. Phys.* **2021**, *154*, 214109.

(4) Ghosh, P.; Alvertis, A. M.; Chowdhury, R.; Murto, P.; Gillett, A. J.; Dong, S.; Sneyd, A. J.; Cho, H.-H.; Evans, E. W.; Monserrat, B.; Li, F.; Schnedermann, C.; Bronstein, H.; Friend, R. H.; Rao, A. Decoupling excitons from high-frequency vibrations in organic molecules. *Nature* **2024**, *629*, 355−362.

(5) Shi, L.; Xie, X.; Troisi, A. Rapid calculation of internal conversion and intersystem crossing rate for organic materials discovery. *J. Chem. Phys.* **2022**, *157*, 134106.

(6) do Casal, M. T.; Veys, K.; Bousquet, M. H. E.; Escudero, D.; Jacquemin, D. First-Principles Calculations of Excited-State Decay Rate Constants in Organic Fluorophores. *J. Phys. Chem. A* **2023**, *127*, 10033−10053.

(7) Bozzi, A. S.; Rocha, W. R. Calculation of Excited State Internal Conversion Rate Constant Using the One-Effective Mode Marcus-Jortner-Levich Theory. *J. Chem. Theory Comput.* **2023**, *19*, 2316−2326.

(8) Marcus, R. A. Electron transfer reactions in chemistry. *Theory and experiment. Rev. Mod. Phys.* **1993**, *65*, 599−610.

(9) Valiev, R. R.; Cherepanov, V. N.; Nasibullin, R. T.; Sundholm, D.; Kurten, T. Calculating rate constants for intersystem crossing and internal conversion in the Franck−Condon and Herzberg−Teller approximations. *Phys. Chem. Chem. Phys.* **2019**, *21*, 18495−18500.

(10) Valiev, R. R.; Nasibullin, R. T.; Cherepanov, V. N.; Kurtsevich, A.; Sundholm, D.; Kurtén, T. Fast estimation of the internal conversion rate constant in photophysical applications. *Phys. Chem. Chem. Phys.* **2021**, *23*, 6344−6348.

(11) Nasibullin, R.; Merzlikin, B.; Valiev, R.; Cherepanov, V. Fast calculation of internal conversion rate constant using the time-dependent formalism. *Chem. Phys. Lett.* **2024**, *840*, No. 141147.

(12) Schnedermann, C.; Liebel, M.; Kukura, P. Mode-Specificity of Vibrationally Coherent Internal Conversion in Rhodopsin during the Primary Visual Event. *J. Am. Chem. Soc.* **2015**, *137*, 2886−2891.

(13) Farag, M. H.; Jansen, T. L. C.; Knoester, J. Probing the Interstate Coupling near a Conical Intersection by Optical Spectroscopy. *J. Phys. Chem. Lett.* **2016**, *7*, 3328−3334.

(14) Meneghin, E.; Leonardo, C.; Volpato, A.; Bolzonello, L.; Collini, E. Mechanistic insight into internal conversion process within Q-bands of chlorophyll a. *Sci. Rep.* **2017**, *7*, 11389.

(15) Boeije, Y.; Olivucci, M. From a one-mode to a multi-mode understanding of conical intersection mediated ultrafast organic photochemical reactions. *Chem. Soc. Rev.* **2023**, *52*, 2643−2687.

(16) Rozzi, C. A.; Troiani, F.; Tavernelli, I. Quantum modeling of ultrafast photoinduced charge separation. *J. Phys.: Condens. Matter* **2018**, *30*, No. 013002.

(17) Nelson, T. R.; White, A. J.; Bjorgaard, J. A.; Sifain, A. E.; Zhang, Y.; Nebgen, B.; Fernandez-Alberti, S.; Mozyrsky, D.; Roitberg, A. E.;

Tretiak, S. Non-adiabatic Excited-State Molecular Dynamics: Theory and Applications for Modeling Photophysics in Extended Molecular Materials. *Chem. Rev.* **2020**, *120*, 2215−2287.
(18) Petropoulos, V.; Rukin, P. S.; Quintela, F.; Russo, M.; Moretti, L.; Moore, A.; Moore, T.; Gust, D.; Prezzi, D.; Scholes, G. D.; Molinari, E.; Cerullo, G.; Troiani, F.; Rozzi, C. A.; Maiuri, M. Vibronic Coupling Drives the Ultrafast Internal Conversion in a Functionalized Free-Base Porphyrin. *J. Phys. Chem. Lett.* **2024**, *15*, 4461−4467.
(19) Rukin, P.; Prezzi, D.; Rozzi, C. A. Excited-state normal-mode analysis: The case of porphyrins. *J. Chem. Phys.* **2023**, *159*, 244103.
(20) Elber, R.; Karplus, M. Multiple Conformational States of Proteins: A Molecular Dynamics Analysis of Myoglobin. *Sci.* **1987**, *235*, 318−321.
(21) Kitao, A.; Hayward, S.; Go, N. Energy landscape of a native protein: Jumping-among-minima model. *Proteins: Struct., Funct., Bioinf.* **1998**, *33*, 496−517.
(22) Hayward, S.; de Groot, B. L. *Molecular Modeling of Proteins*; Kukol, A., Ed.; Humana Press: Totowa, NJ, 2008; pp. 89−106.
(23) Amadei, A.; Linssen, A. B. M.; Berendsen, H. J. C. Essential dynamics of proteins. *Proteins: Struct., Funct., Bioinf.* **1993**, *17*, 412−425.
(24) Bahar, I.; Lezon, T. R.; Bakan, A.; Shrivastava, I. H. Normal Mode Analysis of Biomolecular Structures: Functional Mechanisms of Membrane Proteins. *Chem. Rev.* **2010**, *110*, 1463−1497.
(25) Costa, M. G. S.; Batista, P. R.; Bisch, P. M.; Perahia, D. Exploring Free Energy Landscapes of Large Conformational Changes: Molecular Dynamics with Excited Normal Modes. *J. Chem. Theory Comput.* **2015**, *11*, 2755−2767.
(26) Hayward, S. A Retrospective on the Development of Methods for the Analysis of Protein Conformational Ensembles. *Protein J.* **2023**, *42*, 181−191.
(27) Kolossváry, I. A Fresh Look at the Normal Mode Analysis of Proteins: Introducing Allosteric Co-Vibrational Modes. *JACS Au* **2024**, *4*, 1303−1309.
(28) Daidone, I.; Amadei, A. Essential dynamics: foundation and applications. *WIREs Computational Molecular Science* **2012**, *2*, 762−770.
(29) Zhu, Y.; Peng, J.; Xu, C.; Lan, Z. Unsupervised Machine Learning in the Analysis of Nonadiabatic Molecular Dynamics Simulation. *J. Phys. Chem. Lett.* **2024**, *15*, 9601−9619.
(30) Peng, J.; Xie, Y.; Hu, D.; Lan, Z. Analysis of bath motion in MM-SQC dynamics via dimensionality reduction approach: Principal component analysis. *J. Chem. Phys.* **2021**, *154*, No. 094122.
(31) Atkins, A. J.; González, L. Trajectory Surface-Hopping Dynamics Including Intersystem Crossing in [Ru(bpy)3]2+. *J. Phys. Chem. Lett.* **2017**, *8*, 3840−3845.
(32) Capano, G.; Chergui, M.; Rothlisberger, U.; Tavernelli, I.; Penfold, T. J. A Quantum Dynamics Study of the Ultrafast Relaxation in a Prototypical Cu(I)−Phenanthroline. *J. Phys. Chem. A* **2014**, *118*, 9861−9869.
(33) Capano, G.; Penfold, T. J.; Röthlisberger, U.; Tavernelli, I. A Vibronic Coupling Hamiltonian to Describe the Ultrafast Excited State Dynamics of a Cu(I)-Phenanthroline Complex. *CHIMIA* **2014**, *68*, 227−230.
(34) Capano, G.; Penfold, T. J.; Chergui, M.; Tavernelli, I. Photophysics of a copper phenanthroline elucidated by trajectory and wavepacket-based quantum dynamics: a synergetic approach. *Phys. Chem. Chem. Phys.* **2017**, *19*, 19590−19600.
(35) He, R.; Li, H.; Shen, W.; Yang, Q.; Li, M. Vibronic fine-structure in the S0→S1 absorption spectrum of zinc porphyrin: A Franck−Condon simulation incorporating Herzberg−Teller theory and the Duschinsky effect. *J. Mol. Spectrosc.* **2012**, *275*, 61−70.
(36) Santoro, F.; Lami, A.; Improta, R.; Bloino, J.; Barone, V. Effective method for the computation of optical spectra of large molecules at finite temperature including the Duschinsky and Herzberg−Teller effect: The Qx band of porphyrin as a case study. *J. Chem. Phys.* **2008**, *128*, 224311.
(37) Bricker, W. P.; Shenai, P. M.; Ghosh, A.; Liu, Z.; Enriquez, M. G. M.; Lambrev, P. H.; Tan, H.-S.; Lo, C. S.; Tretiak, S.; Fernandez-Alberti, S.; Zhao, Y. Non-radiative relaxation of photoexcited chlorophylls: theoretical and experimental study. *Sci. Rep.* **2015**, *5*, 13625.
(38) Shenai, P. M.; Fernandez-Alberti, S.; Bricker, W. P.; Tretiak, S.; Zhao, Y. Internal Conversion and Vibrational Energy Redistribution in Chlorophyll A. *J. Phys. Chem. B* **2016**, *120*, 49−58.
(39) Zheng, F.; Fernandez-Alberti, S.; Tretiak, S.; Zhao, Y. Photoinduced Intra- and Intermolecular Energy Transfer in Chlorophyll a Dimer. *J. Phys. Chem. B* **2017**, *121*, 5331−5339.
(40) Fortino, M.; Collini, E.; Bloino, J.; Pedone, A. Unraveling the internal conversion process within the Q-bands of a chlorophyll-like-system through surface-hopping molecular dynamics simulations. *J. Chem. Phys.* **2021**, *154*, No. 094110.
(41) Falahati, K.; Hamerla, C.; Huix-Rotllant, M.; Burghardt, I. Ultrafast photochemistry of free-base porphyrin: a theoretical investigation of B → Q internal conversion mediated by dark states. *Phys. Chem. Chem. Phys.* **2018**, *20*, 12483−12492.
(42) Reiter, S.; Bäuml, L.; Hauer, J.; de Vivie-Riedle, R. Q-Band relaxation in chlorophyll: new insights from multireference quantum dynamics. *Phys. Chem. Chem. Phys.* **2022**, *24*, 27212−27223.
(43) Cigrang, L. L. E.; Green, J. A.; Gómez, S.; Cerezo, J.; Improta, R.; Prampolini, G.; Santoro, F.; Worth, G. A. Non-adiabatic direct quantum dynamics using force fields: Toward solvation. *J. Chem. Phys.* **2024**, *160*, 174120.
(44) Terazono, Y.; North, E. J.; Moore, A. L.; Moore, T. A.; Gust, D. Base-Catalyzed Direct Conversion of Dipyrromethanes to 1,9-Dicarbinols: A [2 + 2] Approach for Porphyrins. *Org. Lett.* **2012**, *14*, 1776−1779.
(45) Terazono, Y.; Kodis, G.; Chachisvilis, M.; Cherry, B. R.; Fournier, M.; Moore, A.; Moore, T. A.; Gust, D. Multiporphyrin Arrays with $\pi-\pi$ Interchromophore Interactions. *J. Am. Chem. Soc.* **2015**, *137*, 245−258.
(46) Wang, H.-H.; Jiang, Y.-Y.; Mahmood, M. H.; Liu, H.-Y.; Sung, H. H.; Williams, I. D.; Chang, C. K. β-Octafluorinated tetrakis-(ethoxycarbonyl)porphyrin. *Chin. Chem. Lett.* **2015**, *26*, 529−533.
(47) Wang, H.-H.; Liu, H.-Y.; Cheng, F.; Ali, A.; Shi, L.; Xiao, X.-Y.; Chang, C.-K. Silver(II) 5,10,15,20-tetra(ethoxycarbonyl) porphyrin: An unexpected six-coordinate linear assembled structure. *Chin. Chem. Lett.* **2018**, *29*, 1404−1408.
(48) Zhang, Z.; Yu, H.-J.; Wu, S.; Huang, H.; Si, L.-P.; Liu, H.-Y.; Shi, L.; Zhang, H.-T. Synthesis, characterization, and photodynamic therapy activity of 5,10,15,20-Tetrakis(carboxyl)porphyrin. *Bioorg. Med. Chem.* **2019**, *27*, 2598−2608. From controlling chemical bonding to deciphering and manipulating biological processes.
(49) Marcelli, A.; Foggi, P.; Moroni, L.; Gellini, C.; Salvi, P. R. Excited-State Absorption and Ultrafast Relaxation Dynamics of Porphyrin, Diprotonated Porphyrin, and Tetraoxaporphyrin Dication. *J. Phys. Chem. A* **2008**, *112*, 1864−1872.
(50) Tomasi, J.; Mennucci, B.; Cammi, R. Quantum Mechanical Continuum Solvation Models. *Chem. Rev.* **2005**, *105*, 2999−3094.
(51) Frisch, M. J. et al. *Gaussian 16 Revision C.01*; Gaussian Inc.: Wallingford CT, 2016.
(52) Petrenko, T.; Neese, F. Analysis and prediction of absorption band shapes, fluorescence band shapes, resonance Raman intensities, and excitation profiles using the time-dependent theory of electronic spectroscopy. *J. Chem. Phys.* **2007**, *127*, 164319.
(53) Yurenev, P. V.; Kretov, M. K.; Scherbinin, A. V.; Stepanov, N. F. Environmental Broadening of the CTTS Bands: The Hexaammineruthenium(II) Complex in Aqueous Solution. *J. Phys. Chem. A* **2010**, *114*, 12804−12812.
(54) Kretov, M. K.; Iskandarova, I. M.; Potapkin, B. V.; Scherbinin, A. V.; Srivastava, A. M.; Stepanov, N. F. Simulation of structured 4T1→6A1 emission bands of Mn2+ impurity in Zn2SiO4: A first-principle methodology. *J. Lumin.* **2012**, *132*, 2143−2150.
(55) Kretov, M. K.; Scherbinin, A. V.; Stepanov, N. F. Simulating the structureless emission bands of Mn2+ ions in ZnCO3 and CaCO3

https://doi.org/10.1021/acs.jctc.4c00698
J. Chem. Theory Comput. XXXX, XXX, XXX−XXX

matrices by means of quantum chemistry. *Russ. J. Phys. Chem. A* **2013**, *87*, 245−251.
(56) Rukin, P. S.; Freidzon, A. Y.; Scherbinin, A. V.; Sazhnikov, V. A.; Bagaturyants, A. A.; Alfimov, M. V. Vibronic bandshape of the absorption spectra of dibenzoylmethanatoboron difluoride derivatives: analysis based on ab initio calculations. *Phys. Chem. Chem. Phys.* **2015**, *17*, 16997−17006.
(57) Penfold, T. J.; Eng, J. Mind the GAP: quantifying the breakdown of the linear vibronic coupling Hamiltonian. *Phys. Chem. Chem. Phys.* **2023**, *25*, 7195−7204.
(58) Small, G. J. Herzberg−Teller Vibronic Coupling and the Duschinsky Effect. *J. Chem. Phys.* **1971**, *54*, 3300−3306.
(59) Shuai, Z.; Geng, H.; Xu, W.; Liao, Y.; André, J.-M. From charge transport parameters to charge mobility in organic semiconductors through multiscale simulation. *Chem. Soc. Rev.* **2014**, *43*, 2662−2679.
(60) Casotto, A.; Rukin, P. S.; Fresch, E.; Prezzi, D.; Freddi, S.; Sangaletti, L.; Rozzi, C. A.; Collini, E.; Pagliara, S. Coherent Vibrations Promote Charge-Transfer across a Graphene-Based Interface. *J. Am. Chem. Soc.* **2024**, *146*, 14989−14999.
(61) Frank-Kamenetskii, M. D.; Lukashin, A. V. Electron-vibrational interactions in polyatomic molecules. *Phys. Usp.* **1975**, *18*, 391−409.
(62) Cederbaum, L. S.; Köppel, H.; Domcke, W. Multimode vibronic coupling effects in molecules. *Int. J. Quantum Chem.* **1981**, *20*, 251−267.
(63) Subotnik, J. E.; Ouyang, W.; Landry, B. R. Can we derive Tully's surface-hopping algorithm from the semiclassical quantum Liouville equation? Almost, but only with decoherence. *J. Chem. Phys.* **2013**, *139*, 214107.
(64) Jain, A.; Sindhu, A. Pedagogical Overview of the Fewest Switches Surface Hopping Method. *ACS Omega* **2022**, *7*, 45810−45824.
(65) Barbatti, M.; Sen, K. Effects of different initial condition samplings on photodynamics and spectrum of pyrrole. *Int. J. Quantum Chem.* **2016**, *116*, 762−771.
(66) Tapavicza, E.; Tavernelli, I.; Rothlisberger, U. Trajectory Surface Hopping within Linear Response Time-Dependent Density-Functional Theory. *Phys. Rev. Lett.* **2007**, *98*, No. 023001.
(67) Plasser, F.; Crespo-Otero, R.; Pederzoli, M.; Pittner, J.; Lischka, H.; Barbatti, M. Surface Hopping Dynamics with Correlated Single-Reference Methods: 9H-Adenine as a Case Study. *J. Chem. Theory Comput.* **2014**, *10*, 1395−1405.
(68) Meyer, T.; Ferrer-Costa, C.; Perez, A.; Rueda, M.; Bidon-Chanal, A.; Luque, F. J.; Laughton, C. A.; Orozco, M. Essential Dynamics: A Tool for Efficient Trajectory Compression and Management. *J. Chem. Theory Comput.* **2006**, *2*, 251−258.
(69) Barbatti, M.; et al. Newton-X Platform: New Software Developments for Surface Hopping and Nuclear Ensembles. *J. Chem. Theory Comput.* **2022**, *18*, 6851−6865.
(70) Plasser, F.; Barbatti, M.; Aquino, A. J. A.; Lischka, H. Excited-State Diproton Transfer in [2,2'-Bipyridyl]-3,3'-diol: the Mechanism Is Sequential, Not Concerted. *J. Phys. Chem. A* **2009**, *113*, 8490−8499.
(71) Quantitative differences with the results published in ref. bib6419 are due to the different minimum used there, i.e., Q_y minimum. This different choice for $q = 0$ does not affect our qualitative results.

https://doi.org/10.1021/acs.jctc.4c00698
J. Chem. Theory Comput. XXXX, XXX, XXX−XXX